Free Surface Elevation Estimator as a Sensor for Wave-Powered Data Buoys

Iain McLeod, Brendan Walsh, Thomas Kelly, and John V. Ringwood, *Fellow, IEEE*

***Abstract*—There is a common perception when monitoring ocean waves, that data buoys, measuring parameters, such as significant wave height and dominant period, must have the characteristics of true wave followers, where the movement of the device is assumed to follow the free surface of the ocean. This presents an obstacle to using wave energy to power data buoys, as wave energy converters necessarily interact with passing waves to harness their energy. This study proposes a Kalman filter-based unknown input estimator to be used as a soft sensor to process readings from an existing motion sensor mounted a data buoy, taking into account the effects of an internal moonpool acting as an oscillating water column (OWC), including tests with an orifice plate to simulate a turbine power take-off (PTO). The estimator described in this article is tested against wave tank data in both regular and irregular waves, for a fully sealed moonpool, acting as a linear system. This article also describes how the Kalman filter can be extended to handle the nonlinearities introduced by fitting an orifice plate simulating an OWC turbine PTO, and tests this against regular wave data. The proposed sensor is found to accurately return values for significant wave height and zero-crossing period, as well as time series estimates of the free surface elevation, at 0.1 s time steps, for both linear and nonlinear system representations.**

***Index Terms*—Data buoys, Kalman filter, ocean sensing, oscillating water column (OWC), unknown input estimation.**

Abbreviations

BEM	Boundary element method.
DkIT	Dundalk institute of technology.
DoFs	Degrees of freedom.
GoF	Goodness of fit.
IMU	Inertial measurement unit.
KFHO	Kalman filter with harmonic oscillator.
(E)KFRW	(Extended) Kalman filter with random walk.
MPC	Model predictive control.
NRMSE	Normalized root-mean-squared error.
NOTF	National ocean test facility.
OWC	Oscillating water column.
PTO	Power take-off.
RHE	Receding horizon estimation.
SNAME	Society of naval architects and marine engineers.
SWL	Still water level.
UIO	Unknown input observer.
WEC	Wave energy converter.

Symbols

A_{ori}	Cross-sectional area of orifice.
A_{owc}	Cross-sectional area of OWC chamber.
a_r	Radiation added mass.
a	Infinite frequency added mass.
b_r	Radiation damping.
c	Hydrostatic stiffness.
f_{ex}	Wave excitation force.
f_{hs}	Hydrostatic restoring force.
f_{pto}	Force from PTO emulator.
f_r	Wave radiation force.
f_{rc}	Force from radiation convolution term.
h_0	Initial height of water column in OWC.
H_s	Significant wave height.
H_{m0}	Spectral domain approximation of H_s.
k_r	Radiation kernel impulse response function.
k_{ex}	Excitation kernel impulse response function.
η	Free surface elevation.
p_{atmos}	Atmospheric pressure.
p	Moonpool pressure.
ρ_{air}	Density of air.
q	Volumetric flow rate.
Q	Process noise covariance matrix.
R	Measurement noise covariance matrix.
T_d	Dominant period.
T_z	Zero-crossing period.
Y_e	States relating to f_{ex} approximation.
Y_{rc}	States relating to f_{rc} approximation.
$z, \dot{z}, \ddot{z}$	Displacement, velocity and acceleration in heave direction.

Subscripts

$3, 33$	Terms relating to the heave mode of the floating buoy, numbered following SNAME convention.
$7, 77$	Terms relating to the piston mode of the OWC.
$73, 37$	Terms coupled between DoFs.

Received 24 October 2024; revised 27 January 2025; accepted 23 February 2025. Date of publication 9 May 2025; date of current version 16 July 2025. This work was supported in part by the Marine Institute Eoin Sweeney Scholarship under Grant-Aid Agreement ES/20/003, funded under the Marine Research Programme by the Irish Government and in part by the Lir National Ocean Test Facility, in association with the Sustainable Energy Authority of Ireland through Lir NOTF ORE Industry Access Programme. *(Corresponding author: Iain McLeod.)*

Associate Editor: Y. Zhou.

Iain McLeod and John V. Ringwood are with the Centre for Ocean Energy Research, Maynooth University, W23 F2H Maynooth, Ireland (e-mail: iain.mcleod.2022@mumail.ie; john.ringwood@mu.ie).

Brendan Walsh is with the Department of Civil Engineering, Dundalk Institute of Technology, A91 K584 Dundalk, Ireland (e-mail: brendan.walsh@dkit.ie).

Thomas Kelly is with the Centre for Renewable Energy, Dundalk Institute of Technology, A91 K584 Dundalk, Ireland (e-mail: thomas.kelly@dkit.ie).

Digital Object Identifier 10.1109/JOE.2025.3551018

I. Introduction

DATA buoys are ubiquitous in the field of marine sensing, and are a vital component of the offshore monitoring network required for weather forecasting, aquaculture, or assessing the suitability of wind- and wavefarm sites. Despite myriad applications, one of the most common sensor requirements for data buoys is to measure wave data, through onboard inclinometers, accelerometers, or pressure sensors. Limited by bandwidth, particularly in locations far from shore, spectral data gathered over the chosen wave acquisition time (set by the end user), is used to give an indication of changes in sea state, typically defined by the significant wave height, and the zero-crossing or dominant period. These wave parameters are calculated in the spectral domain, using (1)–(4) given in [1] and [2], with the significant wave height, H_s, theoretically given as the average of the highest 1/3 of the waves, approximated in the spectral domain as H_{mo}

$$H_{mo} = 4\sqrt{m_0} \tag{1}$$

where m_0 is the variance or zero-order moment, of the free surface elevation time series, as given in the following:

$$m_0 = \sum_{\omega_l}^{\omega_u} S(\omega) d(\omega) \tag{2}$$

where $S(\omega)$ is the spectral density for each frequency band and $d(\omega)$ the bandwidth. ω_l and ω_u represent the lower and upper spectral limits, respectively. The dominant period of the sea state, T_d, is calculated simply as the inverse of the identified frequency band with the highest spectral density [1]. Alternatively, the zero-crossing period, T_z, can be calculated using the following:

$$T_z = 2\pi\sqrt{\frac{m_0}{m_2}} \tag{3}$$

with 2π accounting for frequencies in radians, and where m_2 is the second spectral moment

$$m_2 = \sum_{\omega_l}^{\omega_u} S(\omega) d(\omega) \omega^2. \tag{4}$$

It is generally assumed that data buoys designed to monitor waves should be true wave followers, i.e., the frequency response of the buoy is uniform and unitary. The motion of a wave follower is thus assumed to directly correlate with the movement of the free surface. The notion of true wave followers is idealistic, as floating devices will always have some variation in dynamic response with frequency. Data buoys deemed to be wave followers, are therefore designed with high resonant frequencies, significantly higher than the highest expected wave frequency, to minimise colouring their dynamic response to incident waves.

Aside from the challenges surrounding the scalability of wave energy PTOs discussed in [3], the perception that wave data can only be gathered by true wave followers further throws into question the possibility of using wave energy to power data buoys. Wave energy PTOs generally necessitate device dynamics with a resonant frequency close to the expected frequencies of incident waves. Such dynamic behavior is further exaggerated by the introduction of energy maximizing control, where the goal is to actively manipulate the resonant frequency of the device to match the frequency of incoming waves [4], further moving WECs away from the behavior of true wave followers.

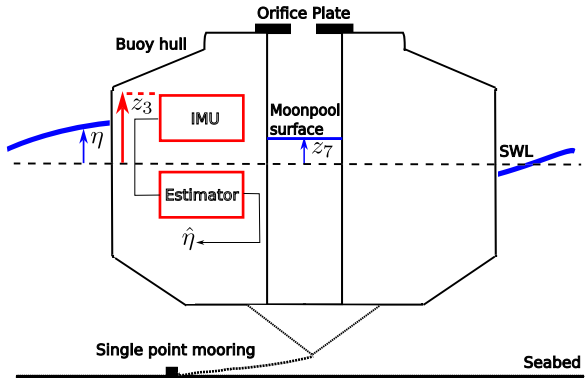

Fig. 1. Schematic showing intended use for estimator on an OWC buoy, with η representing the free surface elevation. The buoy heave motion, z_3, measured by an existing motion sensor, such as an IMU, is fed into the estimator, which then estimates the external free surface elevation, $\hat{\eta}$, accounting for the effects of the first pumping mode of the water column, z_7, on the device dynamics.

This article counters the argument that wave parameters can only be gathered by true wave followers, by proposing a free surface elevation soft sensor, based on Kalman filter-based unknown input estimation techniques, designed to be used in conjunction with an existing motion sensor, such as an IMU, which takes into account the dynamics of an OWC-based data buoy, as shown in Fig. 1. The estimator described in this article is validated against experimental wave tank data, and shown to successfully estimate H_s and T_z from measurements of its heave displacement, with the calculated H_s values falling within a similar error band as the industry standard of H_{mo}, which is known to overpredict H_s by 5% –10% [1].

In addition, the proposed sensor has the capability to return estimates of the free surface elevation. The ability to measure free surface elevation data is essential for the development of large-scale (grid power level) WECs, in particular those fitted with energy maximising control. As previously mentioned, many WEC controllers work on a wave-by-wave basis, tuning the device resonant frequency to match incident waves. Therefore, to validate such controllers, a means of measuring time series free surface elevation is necessary, often limiting such tests to wave tanks, where wave probes can measure the free surface elevation directly.

Although suitable for the majority of current data buoy end-users, using spectral data alone to define wave climates also has broader limitations. As demonstrated in [2], using time-series wave data gathered on the West Coast of Ireland, very different spectral shapes can have the same variance in spectral density and thus be described by the same values of H_{mo} and T_z. Furthermore, Nolan et al. [2] showed that, where H_{mo} and T_z are used to describe wave climates, which are in fact double peaked spectra, T_z can correlate with a frequency band with a low spectral density. Particularly, for WECs, such shortcomings can have severe implications at the design stage, where device

resonant frequency is often designed around the stated T_z of the location where it is to be deployed.

In [5], the dearth of recorded time-series free surface elevation data are discussed in detail, with Collins III et al. [5] specifically addressing the issues that buoy tilt can cause for acceleration measurements in the time domain. Indeed, elsewhere in the literature, when time domain free surface elevation is addressed, it tends to relate to improving the time series accumulation of measurements used to calculate the stated statistical characteristic parameters of H_{mo} and T_z. A recent example is [6], which focuses on a number of gap filling methods, using both nonlinear data driven methods and linear methods to impute time-domain data. Gaps filled by the approach in [6] are where anomalous or missing data are found, caused either through sensor failure, or where extreme waves cause the device to become submerged and deviate from its wave-following characteristics, resulting in underestimation of H_{mo}. Chakraborty et al. [6] considered a number of wave prediction methods as a foundation for the work, and indeed it is in wave prediction, rather than measurement, where Kalman filters are most often used in wave measurement applications. Examples, such as [7] or [8], use Kalman filters to predict wave elevation, but in both cases assume that free surface elevation is a directly measurable quantity. Kalman filters have also been used for significant wave height estimation on fixed platforms where the free surface elevation is not measured directly, such as in [9], where wind speed measurements are used to estimate significant wave height of the surrounding seastate. However, the use of Kalman filters in estimating free surface elevation directly remains uncommon in the literature.

In the field of maritime shipping, there is a wealth of studies combining Kalman filters with IMU readings. Primarily, based around estimating the heave motion of the vessel itself, particularly for offshore service vessels or subsea lifting operations, IMUs have been successfully used in conjunction with Kalman filters as part of the control system for onboard heave compensation systems [10], [11]. A recent study [12] broadens the application of the Kalman filter to estimate the geoid height of the vessel, in this case using the Kalman filter to facilitate sensor fusion between the onboard IMU and global navigation satellite systems data.

The advent of autonomous ships is also driving a demand for time series free surface elevation data. A number of papers have been published, similarly using Kalman filter-based unknown input estimators, to obtain not only free surface elevation, but also directional wave spectra, from sensors located across a 70 m long vessel [13], [14], [15], [16]. Such an overlap of interests, between the maritime shipping and wave energy sectors, could build momentum in improving sensor technology for returning time-series free surface elevation, which has so far been a mostly niche requirement of the wave energy research community.

The rest of this article is organized as follows. Section II gives a brief description of the data buoy used, alongside details of the experimental setup used for wave tank testing. Section III describes the design of the free surface estimator and the related hydrodynamic models. Section IV discusses the validation of both the hydrodynamic models and the estimator against experimental data. Note that Sections III and IV are split between the case considering a fully sealed chamber, resulting in a linear system, and the nonlinear case with a 25-mm orifice plate. Finally, Section V concludes this article by reflecting on the key findings of this article and suggesting potential future work.

II. System Description

The buoy used as the basis for the OWC in this study is a JFC Marine Gannet G1250 buoy, with a diameter of 1.25 m and a nominal draft of 0.58 m (schematics and full technical details are available from JFC Marine [17]). The centre core of the buoy has been left open at the base creating a moonpool that acts as an OWC. The dimensions of the moonpool in the centre are a diameter of 0.18 m with a height of 1 m. This off-the-shelf JFC Marine buoy, with a moonpool chamber, has previously been used in a wave measurement capacity as part of the wave activated sensor power buoy project at DkIT [18], [19], [20]. Indeed, Walsh et al. [20] made use of the results from the same experimental data described in Section II-A, developing a successful technique for estimating wave spectra based on frequency domain transfer functions obtained relating the pressure spectra in the fully sealed moonpool chamber to the external wave spectrum. One other important distinction is this article's focus on time-domain techniques, in contrast to the frequency-domain technique of [20]. Where the focus of Walsh et al. [20] was on obtaining the statistical characteristic parameters of waves from the pressure spectra across half hour windows, the primary objective, and novelty, of this article is in the design of an unknown input estimator which can return time domain free surface readings at 0.1 s time steps, based on measurements of the device heave motion.

Alongside a fully sealed plate, a number of orifice plates, representing the turbine PTO at the top of the OWC, were alternatively attached to the top of the moonpool chamber. In Section II-A, the experimental set up for wave tank testing of the buoy at the Lir NOTF in Cork is discussed, with Section II-B describing the experimental set up at DkIT for determining the coefficient of discharge for the 25 mm orifice plate.

A. Experimental Set Up in Wave Tank

To obtain experimental results the G1250 was tested at the Lir NoTF, using the deep ocean basin (35 m × 12 m × 3 m deep). The tests carried out used a fully sealed moonpool, initially tested in regular waves, and then tested in irregular waves, based on a scaled Brettschneider spectrum of sea states observed at Galway Bay.

To represent a turbine PTO, the moonpool was also fitted with a number of orifice plates, with orifice diameters of 5, 15, and 25 mm, which were tested in regular waves. All tests used a single point mooring.

Waves in the basin were measured using three resistive wave probes, placed between the wave maker and the buoy, as illustrated in Fig. 2, and a pressure sensor was fitted to the plate covering the top of the moonpool to record the internal pressure of the OWC. The displacement of the buoy was measured using a Qualisys motion capture system, which records data in 6 DoFs. A steel mass was added to the top of the buoy

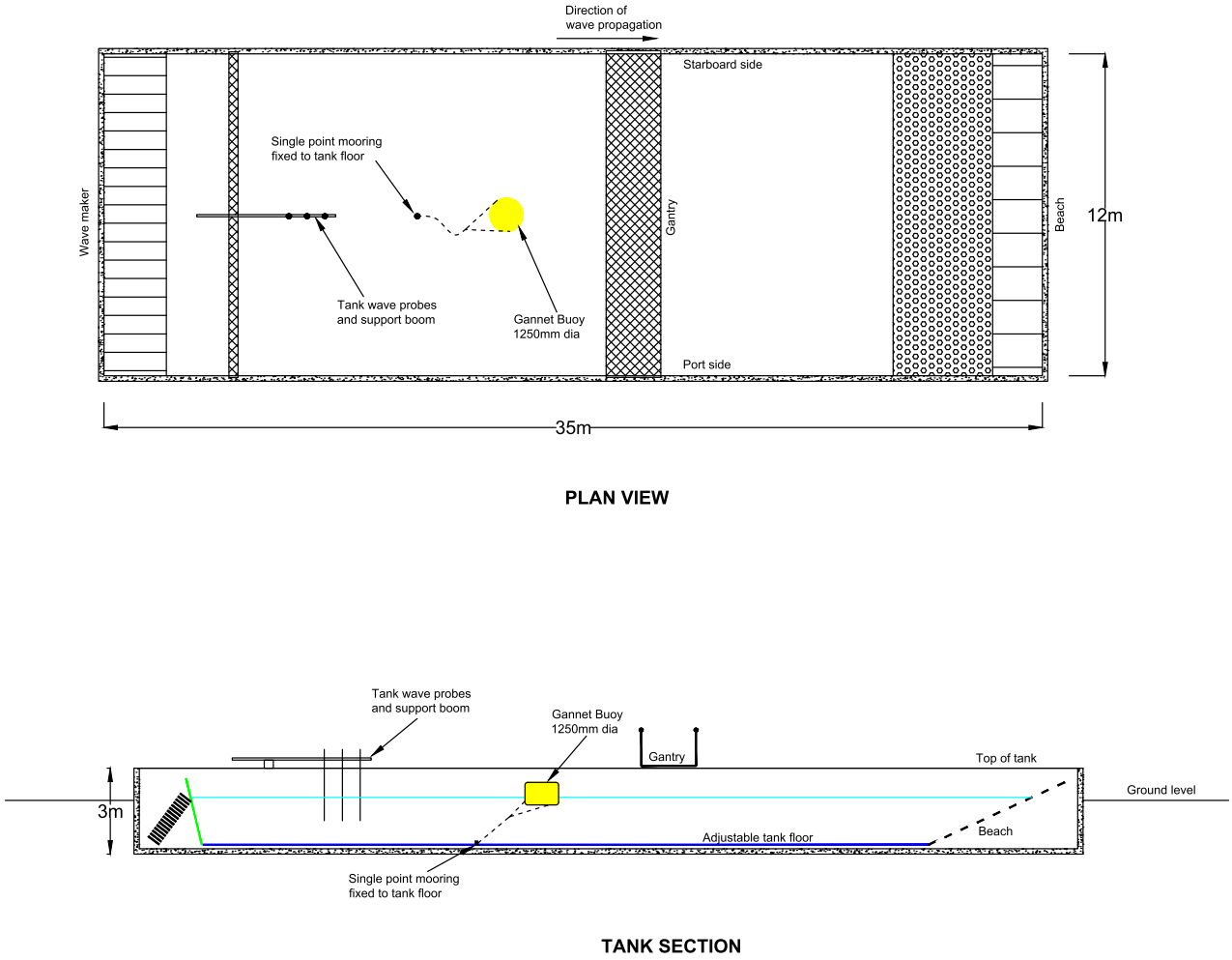

Fig. 2. Plan view and section view of wave tank testing layout at Lir NOTF, showing the position of wave probes, wavemaker, and the mooring location of the G1250 Gannet buoy.

to represent the onboard batteries, as shown in Fig. 3. In this article, only motion measurements are considered, because of well-known implementation issues when using pressure sensors with estimators [21].

To test and validate the free surface elevation estimator, the tests using the sealed moonpool are chosen, as both regular and irregular wave data are available. Furthermore, if the air inside the moonpool is assumed to be incompressible, the fully sealed chamber also results in a relatively simple linear system. The 25-mm orifice tests are selected, as the largest diameter orifice has the most significant impact on the dynamics of the device, compared to the sealed case, introducing nonlinearities through the orifice equation and the effects of air compressibility. Although no irregular wave tests were carried out with the orifice plates at Lir NOTF, synthetic data has been generated to assess the ability of the nonlinear estimator to handle irregular waves.

B. Experimental Determination of Coefficient of Discharge

After obtaining test results at Lir NOTF, a second set of experiments was carried out at the DkIT wave flume (18 m $\times$ 0.35 m $\times$ 1 m deep), to determine the value of the coefficient of discharge, C_d, from the 25 mm orifice, following the approach in [22].

This experimental setup uses a sealed wooden chamber, open at the base, and with a hole in the top aligning with the orifice in the plate, which is lowered into the water of the wave tank, allowing the chamber to partially fill. The orifice plate is attached to the opening on top of the chamber with a wave probe to measure free surface elevation inside the chamber and a pressure sensor to measure pressure variation, shown in Fig. 4.

Low frequency waves, from 0.4 to 0.7 Hz with an amplitude of 30 mm, are then used to generate a series of measurements, where the free surface inside the chamber remains close to parallel with the orifice plate, allowing the volumetric flow rate, q, through the orifice to be calculated using the following:

$$q = A_{\text{owc}}\dot{\eta}_{\text{owc}} \tag{5}$$

where A_{owc} is the cross-sectional area of the OWC chamber and $\dot{\eta}_{\text{owc}}$ is the differentiated signal of the free surface elevation within the chamber, measured via the wave probe.

The orifice equation, given by (6), then allows the resultant values to be plotted against the volumetric flow rate as given in

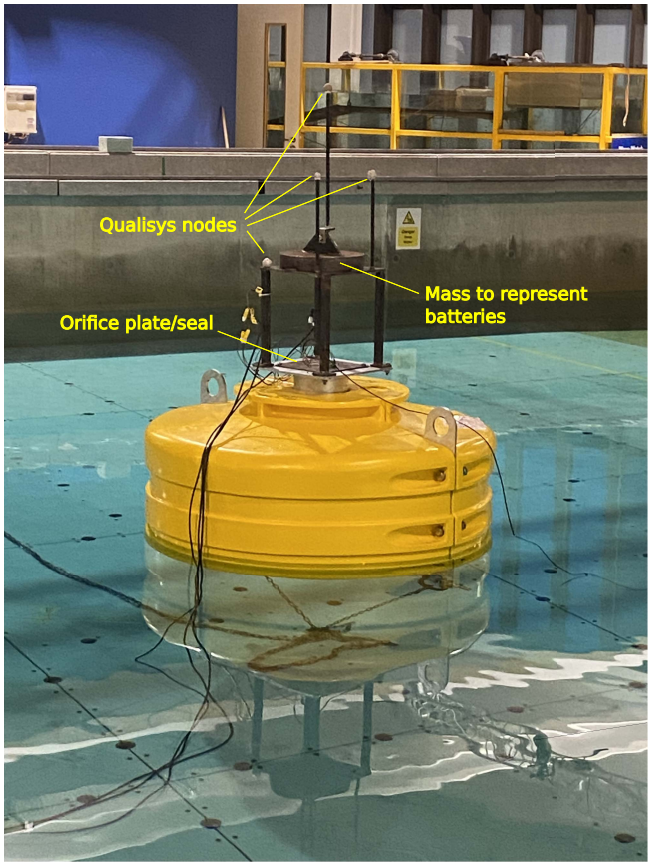

Fig. 3. Experimental set up at Lir NOTF, using a single point mooring, a mass to represent the batteries, and the orifice plate or seal with fitted pressure sensor.

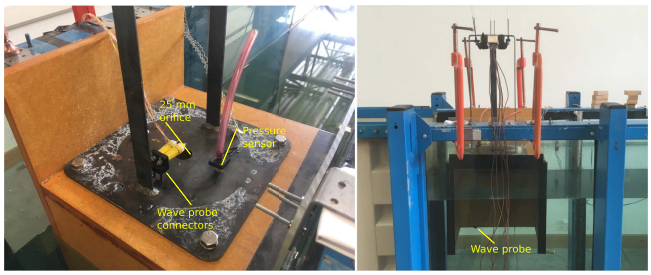

Fig. 4. Experimental set up for determining C_d, using a pressure sensor and a single wave probe in a wooden chamber with the 25 mm orifice plate attached to the opening at the top.

the following:

$$q = \frac{A_{\text{ori}}\sqrt{2\rho_{\text{air}}\Delta p}}{\rho_{\text{air}}} \tag{6}$$

where A_{ori} is the orifice area, ρ_{air} the density of the air within the chamber, and Δp is the difference between the pressure within the chamber and the atmospheric pressure outside the chamber.

The gradient of the resultant plot, shown in Fig. 5, gives an experimental value for C_d. The obtained values are slightly higher than the benchmark of approximately 0.6 expected of a sharp-edged orifice. All sensors were calibrated, and the tests repeated to eliminate the possibility of errors in the sensors, confirming the value of $C_d = 0.71$ for the 25 mm orifice.

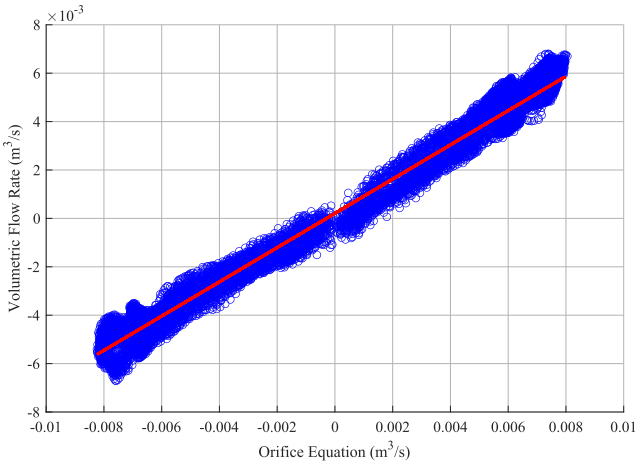

Fig. 5. Determination of C_d from experimental results, plotting volumetric flow rate, q, against the orifice equation (6).

III. Designing the Free Surface Elevation Estimator

This section is split between the development of the hydrodynamic models used by the free surface elevation estimator, and the design of the free surface elevation estimator itself. The Kalman filter-based estimator is highly reliant on the model of the system, and thus these two aspects of the design process are closely linked. Section III-A describes the hydrodynamic model, beginning with the steps required to ensure that the input to the model is the free surface elevation, alongside the steps required to represent the system in state space form: with Sections III-A1 and III-A2 describing the differences between the linear and the nonlinear system respresentations, respectively. Section III-B follows a similar format, describing the incorporation of the hydrodynamic state space models in the estimator structure, with Section III-B1 describing the linear estimator, and Section III-B2 the nonlinear estimator.

A. Hydrodynamic Modeling

For this system, the unknown input is the free surface. The modeling of the system focuses on the displacement in the heave direction, z, allowing the dynamics of the system in the time domain to be represented as follows:

$$M\ddot{z}(t) = f_{\text{ex}} + f_r + f_{\text{hs}} + f_{\text{pto}} \tag{7}$$

where M is the mass of the buoy, f_{ex} is the excitation force, f_r is the radiation force, f_{hs} is the hydrostatic restoring force, and f_{pto} is the force from the orifice plate emulating the PTO. Forces that were not captured in the hydrodynamic models used for the free surface elevation estimator are the viscous drag force, due to the linear flow theory assumptions discussed below, and the force from the mooring lines, which are highly nonlinear and come with a significant computational cost.

In this article, a Cummins' equation-based approach is used, as this is a relatively simple method of modeling the dynamics of a system. This simplicity does come with a number of caveats which must be noted, pertaining to the linear flow theory assumptions required for using the Cummins' equation. It must

be assumed that the fluid is incompressible; in the case of the OWC, this assumption need only be applied to the water upon which the body is floating and, as discussed in Section III-A2, air compressibility effects can still be accounted for. The water particles are assumed to be irrotational, thereby implying the water is also inviscid. Finally, the device motion must be small compared to its dimension, and the wave amplitude small with respect to the wavelength. With the OWC PTO being modeled only through an orifice plate, there is no additional energy injected into the system through the PTO simulator, which should ensure device motions remain small.

To obtain the frequency dependent terms of radiation added mass, a_r, radiation damping, b_r, and the excitation force frequency response function, H_{ex}, the BEM solver WAMIT was used. As linear potential flow theory is used for hydrodynamic modeling, only the submerged part of the G1250 is modeled in AutoCAD, and meshed in MultiSurf. WAMIT is one of the few BEM solvers that can handle OWCs. By modeling the surface of the water within the moonpool as an infinitely thin massless disc [23], the water surface within the chamber can be set as the top patch in the BEM solver. As this top patch is normally what enables the irregular frequency removal tool, this function becomes unavailable with OWCs. So-called "irregular frequencies" in BEM solvers refer to anomalous spikes in magnitude in the results for added mass and radiation damping. Removal of "irregular frequencies" therefore must be carried out manually following the methods outlined in [24].

Another issue that occurs with the massless disc modelling approach for OWCs is that values obtained for added mass at higher frequencies tend toward negative infinity, rather than converging toward a finite value for infinite frequency added mass, a. Thus, the added mass needs to be reconstructed from the radiation damping using the Ogilvie relations, given as follows:

$$a_r(\omega) = a - \frac{1}{\omega}\int_0^\infty k_r(t)\sin(\omega t)dt \tag{8}$$

$$b_r(\omega) = \int_0^\infty k_r(t)\cos(\omega t)dt \tag{9}$$

where $k_r(t)$ is the radiation impulse response function in the time domain. Equation (9) can then be used to express $k_r(t)$ only in terms of the radiation damping terms

$$k_r(t) = \frac{2}{\pi}\int_0^\infty b_r(\omega)\cos(\omega t)d\omega. \tag{10}$$

Following the method outlined in [24], "irregular frequencies" are removed from the radiation damping results, which are then used to reconstruct the added mass curves. A limitation of reconstructing added mass in this way, is that any offset of added mass on the vertical axis is removed, meaning an initial estimate for a_∞ must be adjusted manually until the reconstructed added mass overlaps with the lower frequency added mass values from WAMIT, as demonstrated in Fig. 6.

To convert the excitation force input from Cummins' equation to free surface elevation, the excitation force impulse response kernel, k_{ex}, is approximated as a separate state space system. In the time domain, free surface elevation, η, is related to excitation

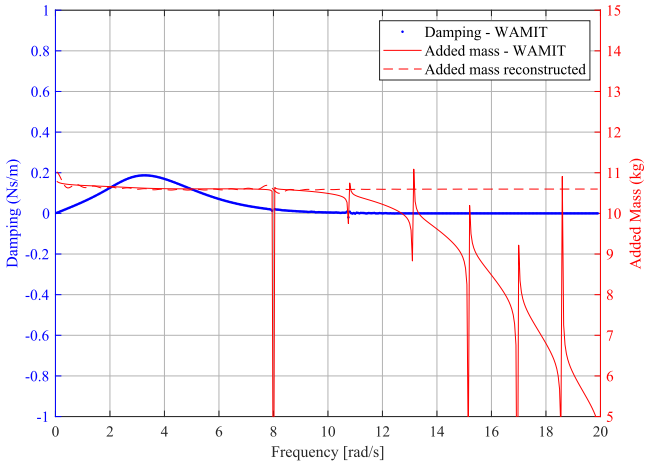

Fig. 6. Added mass for the piston mode of the water column in the OWC chamber, reconstructed from the radiation damping to correct the trend toward $-\infty$, which is symptomatic of the massless disc approximation approach. Also achieved is the removal of the anomalous spikes in magnitude known as "irregular frequencies."

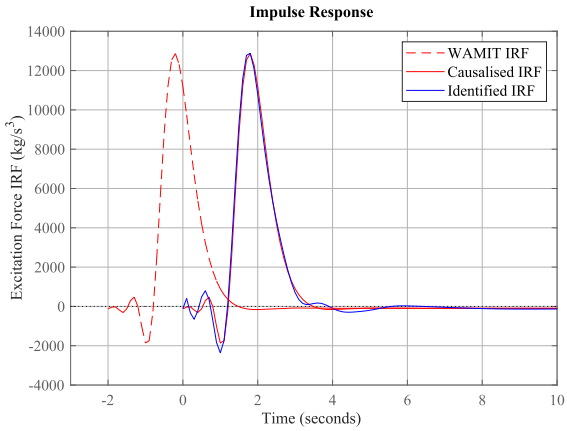

Fig. 7. Comparison of the noncausal impulse response function obtained from the WAMIT results, and the subsequent causalization and the impulse response from the identified state space approximation.

force by

$$f_{\text{ex}}(t) = k_{\text{ex}}(t)^*\eta(t) = \int_{-\infty}^{\infty} k_{ex}(t-\tau)\eta(\tau)d\tau \tag{11}$$

where $*$ is the convolution operator.

The excitation force kernel, or impulse response function, k_{ex}, is defined by the following:

$$k_{\text{ex}}(t) = \frac{1}{2\pi}\int_{-\infty}^{\infty} H_{\text{ex}}(j\omega)e^{j\omega t}d\omega \tag{12}$$

where H_{ex} is the excitation force frequency response function obtained from WAMIT.

Due to the manner in which the reference frame for modeling the hydrodynamics of floating bodies is chosen, most commonly set at the centre of the device, the excitation force acting on the device is assumed to be due to the wave elevation at the centre of the device, resulting in a noncausal process [25]. The resulting noncausality can be observed in Fig. 7, where k_{ex} has both a component before t = 0 s and after. To approximate a

state space equivalent, without losing dynamic information, k_{ex} is casualized by following the method outlined in [26], where k_{ex} is shifted by a casualization time, t_c, until there is no significant component below 0 s, affecting the relationship between k_{ex} and η, as described as follows:

$$\begin{aligned} f_{\text{ex}} &= k_{\text{ex}}(t)^{*}\eta(t) \\ &= k_{\text{ex}}\left(t-t_c\right)^{*}\eta\left(t+t_c\right). \end{aligned} \tag{13}$$

As demonstrated by (13), causalizing k_{ex} introduces a timeshift in the related free surface elevation equal to the casualization time. To generate a state space approximation of the causalized excitation kernel, a Hankel singular value decomposition is used to reduce the impulse response function to an order suitable for inclusion in the model (in this case order 10). Equation (13) can then be approximated in state space form as follows:

$$\begin{aligned} \dot{Y}_e(t) &= A_e Y_e(t) + B_e \eta(t+t_c) \\ f_{ex} &\approx C_e Y_e(t) \end{aligned} \tag{14}$$

where Y_e refers to the states required for the excitation force approximation. The approximated state space model was then excited with an impulse signal, to ensure the response of the reduced system matched the original closely, as shown in Fig. 7.

According to Cummins' equation, the radiation force is given as follows:

$$f_r = -a\ddot{z} - k_r * \dot{z}. \tag{15}$$

Defining f_{rc} as

$$f_{\text{rc}} = k_r * \dot{z} \tag{16}$$

allows for (7) to be rewritten as

$$(M+a)\ddot{z}(t) = f_{\text{ex}} + f_{\text{rc}} + f_{\text{hs}} + f_{\text{pto}}. \tag{17}$$

The radiation convolution integral given in (16) is a drawback of using Cummins' equation, as significant computational effort is required to solve it. To overcome the issues associated with the radiation convolution integral, f_{rc} (similarly to f_{ex}) can also be approximated as a finite order state space system, this time following the moment matching approach facilitated by the FOAMM toolbox [27]. This approximates the radiation convolution integral as a separate state space system of the form shown as follows:

$$\begin{aligned} \dot{Y}_{\text{rc}}(t) &= A_{\text{rc}} Y_{\text{rc}}(t) + B_{\text{rc}} \dot{z}(t) \\ f_{\text{rc}} &\approx C_{\text{rc}} Y_{\text{rc}}(t) \end{aligned} \tag{18}$$

where Y_{rc} represents the states required for the radiation convolution term approximation.

The hydrostatic force, f_{hs}, is simply calculated as follows:

$$f_{\text{hs}} = -cz(t) \tag{19}$$

where c is the hydrostatic stiffness.

The force from the PTO emulator, f_{pto}, is handled differently for the sealed chamber and the orifice plate, as described in Sections III-A1 and III-A2, respectively.

For both cases, only those DoFs acting in the heave direction are considered: namely, the heave motion of the buoy itself, and the first heave mode of the massless disc representing the water column inside the chamber, also known as the piston or pumping mode, which are the main power generating DoFs of a floating OWC. The numbering convention used in this article follows that of the SNAME, which number the translational DoFs surge, sway and heave as 1, 2, and 3, and the rotational DoFs roll, pitch and yaw, as 4, 5, and 6, respectively. Hence, the heave mode of the buoy itself is referred to as DoF 3 in this study. As the piston mode of the water column inside the moonpool represents an additional DoF, when describing OWCs, it is common to label this additional DoF as 7 [28], a convention which is followed in this study.

Considering only the buoy motion acting in the heave direction is a limitation of this study, but was adopted to primarily examine the feasibility of this approach. As Section III-A2 shows, the inclusion of DoFs 3 and 7 imparts significant computational cost on the estimator. Adding further DoFs to the dynamic model used by the estimator could be considered in future research. An initial assumption was made that heave is the DoF most closely correlated with the free surface in the tests considered. To assess the validity of this assumption, forward selection was used to determine which DoFs are most affected by the free surface elevation. Forward selection is a common input selection method used in system identification, with applications in both linear and nonlinear modeling [29]. Forward selection is a useful tool for ascertaining the correlation between a set of inputs, in this case, the DoFs surge, heave and pitch, and an output, in this case, free surface elevation. To identify those inputs upon which the output is most dependent, a test criterion must be established, with a chi-squared test used for this study. Forward selection starts from a null model and sequentially selects features from the input set that improve the fit to the test criteria [30].

For the forward selection procedure, a generalized linear model (GLM) was used to relate the free surface elevation to a matrix of the surge, heave and pitch DoFs, for the irregular wave tests. A chi-squared test was then determined as the fitting criterion. A 10-fold cross validation was sequentially carried out, comparing the deviance of the GLM with the chosen percentile of the chi-squared fit. In irregular wave tests, the correlation between the DoFs considered and the free surface was relatively low, with heave only selected at the 60th percentile of the chi-squared fit, and the remaining two DoFs only added when the chi-squared fit dropped beneath the 10th percentile. This shows that the correlation between heave and free surface elevation for the tests considered in this article is significantly higher than either pitch or surge, suggesting that the addition of more DoFs would not significantly improve the performance of the estimator in this case. It should, however, be noted that the waves used in experimental testing were relatively benign, and more significant influence from pitch and surge may be observed in real sea conditions.

1) Sealed Moonpool: In the case of the buoy with a fully sealed moonpool, a simple linear system can be obtained for a single DoF, the heave mode of the buoy (DoF 3), providing the air within the chamber is assumed incompressible. This allows

for (17) to be used directly, setting $f_{\text{pto}} = 0$. Defining the heave displacement of the buoy as z_3, allows the sealed moonpool linear system to be written in state space form as follows:

$$\begin{aligned} \dot{x}(t) &= Ax(t) + Bu(t) \\ y(t) &= Cx(t) \end{aligned} \tag{20}$$

where

$$A = \begin{bmatrix} A_e & 0 & 0 & 0 \\ 0 & A_{\text{rc}} & 0 & B_{\text{rc}} \\ 0 & 0 & 0 & 1 \\ \frac{C_e}{M^*_{33}} & \frac{C_{\text{rc}}}{M^*_{33}} & -\frac{c}{M^*_{33}} & 0 \end{bmatrix}$$

$$B = \begin{bmatrix} B_e \\ 0 \\ 0 \\ 0 \end{bmatrix} \quad x = \begin{bmatrix} Y_e \\ Y_{rc} \\ z_3 \\ \dot{z}_3 \end{bmatrix} \quad u = \eta. \tag{21}$$

By including state space approximations for the excitation force and radiation convolution terms, the size of the resultant state space system grows as the order of the approximated terms increases. A compromise of an order 10 approximation of f_{ex} and an order 6 approximation of f_{rc} is used.

Thus, a fully linear, relatively simple system description is obtained in state space form, which can be used for the unknown input estimator.

2) 25 mm Orifice Plate: Replacing the seal on the moonpool with an orifice plate immediately introduces nonlinearity into the system. This can be seen in the orifice equation describing the flow of air into and out of the orifice, given by piecewise equation as follows:

$$\dot{m} = \begin{cases} -C_d A_{ori} \sqrt{2\rho_{air}|p - p_{atmos}|}, & \text{if } p > p_{atmos} \\ C_d A_{ori} \sqrt{2\rho_{air}|p_{atmos} - p|}, & \text{if } p < p_{atmos} \\ 0, & \text{if } p = p_{atmos} \end{cases} \tag{22}$$

where $\dot{m}$ is the mass flow rate through the orifice, A_{ori} is the cross-sectional area of the orifice, ρ_{air} is the density of air, and p_{atmos} and p are the atmospheric and moonpool pressures, respectively. Following common practice, the processes within the OWC chamber were assumed to be adiabatic [31].

Both compressible and incompressible cases are considered for the nonlinear system. Introducing air compressibility requires the addition of a step calculating the changing air density, given as follows:

$$\rho_{\text{air}} = \rho_{\text{atmos}} \left(1 + \frac{p}{\gamma p_{\text{atmos}}}\right) \tag{23}$$

where γ is the specific heat ratio for air (assumed to be 1.4).

Following the derivation described in [28], accounting for air compressibility affects the mass flow rate equations in (22), giving the piecewise equation as (24) shown at the bottom of this page, where $\beta = A_{\text{ori}} / A_{\text{owc}}$ .The rate of change of pressure within the chamber, $\dot{p}$, is given by

$$\dot{p} = \frac{c_s^2}{V}\dot{m} - \frac{\gamma p}{V}\dot{V} \tag{25}$$

where c_s is the speed of sound in air, and V is the volume of air inside the OWC chamber, calculated by

$$V = A_{\text{owc}} \ (h_0 - z_7) \tag{26}$$

with h_0 the height of the still water level within the chamber, measured from the bottom of the chamber, and z_7 representing the displacement of the water column inside the chamber.

The addition of the orifice plate requires the consideration of two vertical DoFs in the nonlinear system, the heave of the buoy (DoF 3) and the first heave mode of the massless disc representing the surface of the water column inside the chamber (DoF 7). Cummins' equation for the two DOFs considered in the nonlinear case is given as follows:

$$\begin{aligned} f_{\text{ex}33} = {} & M^*_{33}\ddot{z}_3(t) + f_{\text{rc}33} + c_{33}z_3(t) + \cdots \\ & + f_{\text{rc}37} + a_{37}\ddot{z}_7(t) + \Delta p\,(A_{\text{owc}} - A_{\text{ori}}) + c_{73}z_3(t) \end{aligned} \tag{27}$$

$$\begin{aligned} f_{\text{ex}77} = {} & a_{73}\ddot{z}_3(t) + f_{\text{rc}77} + c_{77}z_7(t) + f_{\text{rc}73} + \cdots \\ & + a_{77}\ddot{z}_7(t) + \Delta p A_{\text{owc}} + c_{37}z_7(t). \end{aligned} \tag{28}$$

In (27) and (28), subscripts 3 and 7 refer to their respective DoFs, and any coupling between them, z refers to the displacement in each DoF, a is the infinite frequency added mass, and c the hydrostatic stiffness. The mass of the buoy, and the infinite frequency added mass for the heave mode of the buoy are combined as $M^*_{33} = M + a_{33}$. As rotational modes are ignored in this article, it is assumed that $c_{37} = c_{73} = 0$. Following the same methodology described in Section III-A, separate state space approximations for the excitation force transfer functions relating to both DOFs are found. Similarly, radiation convolution terms for DoFs 3 and 7, as well as the coupled radiation convolution terms were found. The coupled radiation terms $f_{\text{rc}37}$ and $f_{\text{rc}73}$, were found to have almost identical state space approximations. Therefore to simplify the state space matrices in (29) shown at the bottom of the next page, $f_{\text{rc}73}$ has been used to represent both $f_{\text{rc}73}$ and $f_{\text{rc}37}$. The infinite frequency added mass for the coupled terms was similarly found to be equal, with a_{73} used to represent the coupled infinite frequency added mass between DoFs 7 and 3.

The nonlinearity becomes most obvious when the full system is written out in state space format (29), since describing the behavior of the OWC with an orifice plate requires multiplication between different states within the system. For brevity, where null matrices occur, they have been written as 0_m, representing

$$\dot{m} = \begin{cases} -\frac{C_d}{\sqrt{1-\beta^4}} A_{\text{ori}} \sqrt{2\rho_{\text{air}} p \left(\frac{\gamma}{\gamma-1}\right) \left[(p_{\text{atmos}}/p)^{(2/\gamma)} - (p_{\text{atmos}}/p)^{(\gamma+1/\gamma)}\right]}, & \text{if } p > p_{\text{atmos}} \\ \frac{C_d}{\sqrt{1-\beta^4}} A_{\text{ori}} \sqrt{2\rho_{\text{air}} p_{\text{atmos}} \left(\frac{\gamma}{\gamma-1}\right) \left[(p/p_{\text{atmos}})^{(2/\gamma)} - (p/p_{\text{atmos}})^{(\gamma+1/\gamma)}\right]}, & \text{if } p < p_{\text{atmos}} \\ 0, & \text{if } p = p_{\text{atmos}}. \end{cases} \tag{24}$$

appropriately dimensioned null matrices, where m is the matrix dimension.

The final shorthand used in (29) is k_M, given as follows:

$$k_M = \frac{M_{33}^* a_{77}}{M_{33}^* a_{77} - {a_{73}}^2}. \tag{30}$$

The large state space representation in (29) shows the complexity added through the introduction of an orifice plate, even for a relatively simple hydrodynamic modeling approach, such as Cummins' equation.

B. Unknown Input Estimator

In wave energy control, unknown input estimators are a well researched topic, as many WEC control strategies, such as MPC, require knowledge of the excitation force [32]. The wave excitation force, f_{ex}, represents the force acting on a body, due only to oncoming waves. For fixed bodies, f_{ex}, can be measured by integrating the pressure from the wave over the submerged body surface. However, for a floating body, excitation force becomes an unmeasurable quantity, as other hydrodynamic forces, such as the wave radiation force, also affect the pressure across the submerged body [21].

In this article, the same techniques studied for estimating excitation force are turned toward estimating free surface elevation in application as a wave sensor for a data buoy. As established in Section III-A, free surface elevation is related to excitation force via k_{ex}. A shortlist of potential unknown input estimation techniques which use the displacement of the device as the measured output, was drawn from those described in [21] as follows.

1) Kalman filter with harmonic oscillator (KFHO).
2) Kalman filter with random walk (KFRW).
3) Unknown input observer (UIO).
4) Receding horizon estimation (RHE).

Although the UIO and RHE approaches have their merits, particularly around obviating the need for a hydrodynamic model, and the UIO's robustness against model uncertainties, the ease

$$A_{nl} = \begin{bmatrix} A_{e7} & 0_m & & & & \\ 0_m & A_{e3} & 0_m & & & \\ & 0_m & A_{rc73} & 0_m & 0_m & \\ \vdots & \vdots & 0_m & A_{rc77} & 0_m & \\ & & 0_m & 0_m & A_{rc33} & \\ 0_m & 0_m & 0_m & 0_m & 0_m & \\ -\frac{a_{73}}{a_{77}}\frac{k_M C_{e7}}{M_{33}^*} & \frac{k_M C_{e3}}{M_{33}^*} & \frac{k_M C_{rc73}}{M_{33}^*}\left(\frac{a_{73}}{a_{77}} - 1\right) & -\frac{a_{73}}{a_{77}}\frac{k_M C_{rc77}}{M_{33}^*} & -\frac{k_M C_{rc33}}{M_{33}^*} & \\ 0_m & & \cdots & & 0_m & \\ \frac{k_M C_{e7}}{a_{77}} & -\frac{a_{73}}{a_{77}}\frac{k_M C_{e3}}{M_{33}^*} & \frac{k_M C_{rc73}}{a_{77}}\left(\frac{a_{73}}{M_{33}^*} - 1\right) & a_{77} & \frac{a_{73}}{a_{77}}\frac{k_M C_{rc33}}{M_{33}^*} & \\ 0_m & & \cdots & & 0_m & \end{bmatrix}$$

$$\begin{bmatrix} \cdots & & & & 0_m \\ \cdots & & & & 0_m \\ 0_m & B_{rc73} & 0_m & B_{rc73} & 0_m \\ 0_m & 0_m & 0_m & B_{rc77} & 0_m \\ 0_m & B_{rc33} & 0_m & 0_m & 0_m \\ 0 & 1 & 0 & 0 & 0 \\ \frac{k_M c_{33}}{M_{33}^*} & 0 & \frac{k_M a_{37} c_{77}}{M_{33}^* a_{77}} & 0 & k_M\left(\frac{A_{\text{ori}}}{M_{33}^*} + \frac{A_{\text{owc}}\left(\frac{a_{37}}{a_{77}} - 1\right)}{M_{33}^*}\right) \\ 0 & 0 & 0 & 1 & 0 \\ \frac{k_M a_{73}}{M_{33}^* a_{77}} & 0 & -\frac{k_M c_{77}}{a_{77}} & 0 & k_M\left(\frac{(A_{\text{owc}} - A_{\text{ori}})a_{73} - A_{\text{owc}} M_{33}^*}{M_{33}^* a_{77}}\right) \\ 0 & 0 & 0 & \frac{\gamma(\Delta p + P_{\text{atmos}})}{h_0 - z_7} & 0 \end{bmatrix},$$

$$B_{nl} = \begin{bmatrix} B_{e7} & 0_m \\ B_{e3} & \\ 0_m & \vdots \\ \vdots & \\ 0_m & 0_m \\ 0 & 0 \\ 0 & 0 \\ 0 & 0 \\ 0 & 0 \\ 0 & \frac{(c)^2}{A_{\text{owc}}(h_0 - z_7)} \end{bmatrix} \quad x_{nl} = \begin{bmatrix} Y_{e7} \\ Y_{e3} \\ Y_{rc73} \\ Y_{rc77} \\ Y_{rc33} \\ z_3 \\ \dot{z}_3 \\ z_7 \\ \dot{z}_7 \\ \Delta p \end{bmatrix} \quad u_{nl} = \begin{bmatrix} \eta \\ \dot{m} \end{bmatrix}. \tag{29}$$

with which Kalman filters can be extended to the nonlinear case ultimately narrows the decision to being between the KFRW and KFHO.

In a KFHO, the unknown input is modeled as a harmonic oscillator, made up of a number of harmonic components, whereas a KFRW models the input as a white noise driven integrator. An in-depth comparison between using a harmonic oscillator and a random walk as the choice of perturbation model for an unknown input estimator is given in [33]. Although the most widely used in the literature, García-Violini et al. [33] clearly demonstrates the issues with using a harmonic oscillator, finding it to be susceptible to spectral amplification, particularly in noisy real sea conditions. The dependence of the harmonic oscillator on prior knowledge of the frequencies of the harmonic components is also demonstrated. Obtaining information on input frequency components can, in theory, be achieved using measurements from wave buoys, but this same approach for a free surface elevation sensor would create a circular problem where a wave buoy relies on knowledge of wave measurements to produce wave measurements. Conversely, a random walk, where no prior information about the wave frequencies is required, presents itself as the natural choice of perturbation model for the Kalman filter, especially when coupled with its resilience to noise and complexity, identified in [33]. The KFRW approach used in the linear case is extended to the nonlinear case as an extended Kalman filter with random walk (EKFRW).

1) Kalman Filter With Random Walk: The KFRW can be described, in discrete time, as follows:

$$\eta^{\text{KFRW}}(k+1) = \eta^{\text{KFRW}}(k) + \epsilon_\eta(k) \tag{31}$$

where η^{KFRW} is the estimate for the free surface elevation, and $\epsilon_\eta(k)$ is a random number, independently and identically distributed in size, which moves the estimate of η^{KFRW} a random step away from its previous value. An augmented version of the model can be described as follows:

$$\begin{aligned} \tilde{x}_\text{a}(k+1) &= A_\text{a}^\text{d}\tilde{x}_\text{a}(k) + \epsilon(k) \\ \tilde{y}(k) &= C_\text{a}\tilde{x}_\text{a}(k) + \mu(k) \end{aligned} \tag{32}$$

where ϵ is the process white noise, with covariance matrix Q, and μ is the measurement white noise, with covariance matrix R.

The augmented matrices for the KFRW are described by (33), with the superscript d denoting that the matrices, described in (21), have been discretized using the zero-order hold method. The matrix C is set so that only the entry corresponding to the heave displacement of the buoy, z_3, is set to 1, setting the measured output $\tilde{y} = z_3$. x refers to the states in the linear model described in (21)

$$\tilde{x}_\text{a} = \begin{bmatrix} \tilde{x} \\ \tilde{\eta}^{\text{KFRW}} \end{bmatrix}, \quad A_\text{a}^\text{d} = \begin{bmatrix} A^\text{d} & B^\text{d} \\ 0 & 1 \end{bmatrix}, \quad C_\text{a} = \begin{bmatrix} C \\ 0 \end{bmatrix}^T \tag{33}$$

with the tilde denoting estimated states. The *a priori* time update estimates, $\tilde{x}_\text{a}^-$ and P^-, can be calculated as follows:

$$\begin{aligned} \tilde{x}_\text{a}^-(k) &= A_\text{a}^\text{d}\tilde{x}_\text{a}(k-1) \\ P^-(k) &= A_\text{a}^\text{d}P(k-1)A_\text{a}^{\text{d}T} + Q \end{aligned} \tag{34}$$

with the *a posteriori* measurement update estimates calculated as follows:

$$\begin{aligned} K(k) &= P^-(k)C_\text{a}^T\left(C_\text{a}P^-(k)C_\text{a}^T + R\right)^{-1} \\ P(k) &= \left(\mathbf{I} - K(k)C_\text{a}\right)P^-(k) \\ \tilde{x}_\text{a}(k) &= \tilde{x}_\text{a}^-(k) + K(k)\left(y(k) - C_\text{a}\tilde{x}_\text{a}^-(k)\right) \end{aligned} \tag{35}$$

where I is an identity matrix equal in size to A_a^d.

2) Extended Kalman Filter With Random Walk: To enable the estimator to handle the nonlinearities introduced by the introduction of an orifice plate, some changes were required. Similar to (33), although in continuous rather than discrete time, the augmented matrices are set up as described in the following:

$$\tilde{x}_\text{a} = \begin{bmatrix} \tilde{x}_{nl} \\ \tilde{\eta}^{\text{KFRW}} \end{bmatrix}, \quad A_\text{a} = \begin{bmatrix} A_{nl} & B_{nl1} \\ 0 & 1 \end{bmatrix}, \quad C_\text{a} = \begin{bmatrix} C \\ 0 \end{bmatrix}^T \tag{36}$$

where matrices A_{nl} and C_{nl} refer to those described in (29), and B_{nl1} refers to the first column of the B_{nl} matrix. This is to separate the estimated input (free surface elevation) from the other input in the nonlinear case (the calculated mass flow rate through the orifice). To include the effects of $\dot{m}$, the second column of the B_{nl} matrix, B_{nl2}, was included in the model used by the estimator. x_{nl} refers to the states relating to the nonlinear model in (29). The *a priori* time update estimates, thus become the following:

$$\begin{aligned} \dot{\tilde{x}}_\text{a}^-(t) &= A_\text{a}\tilde{x}_\text{a}(t) + B_{nl2}\dot{m}(t) \\ \dot{P}^-(t) &= A_\text{a}P(t)A_\text{a} + Q. \end{aligned} \tag{37}$$

A continuous-discrete approach is used for the extended Kalman filter, which, as described in [21], only differs from the Kalman filter in its calculation of the time update estimates. The Runge–Kutta method is used to calculate the solution for (37) across the discretization period, for each individual time step. Using only the final solution of the resultant ordinary differential equation for each timestep, a discretized local linearization of the nonlinear model is achieved. This allows for a discrete measurement update, as given in (35), to still be used with the EKFRW. The measurement update is a key element of the predictor/corrector Kalman filter, as it forms a closed loop, correcting the estimated heave state with the measured heave displacement at each time step. In an open loop estimator, drift in accuracy would be expected over time, as an accumulation of small errors at each time step could become significant. However, in a Kalman filter, with an optimal gain, given by (35), the inclusion of a measurement update to continuously correct the estimate based on measured information ensures that the estimator is robust against errors accrued over time.

IV. Results

In this section, the estimators are validated against the gathered experimental data. As Kalman filter-based estimators are highly model dependent, the hydrodynamic models themselves are first validated against experimental data in Secion IV-A, before analysing the results of the estimated free surface elevation in Section IV-B.

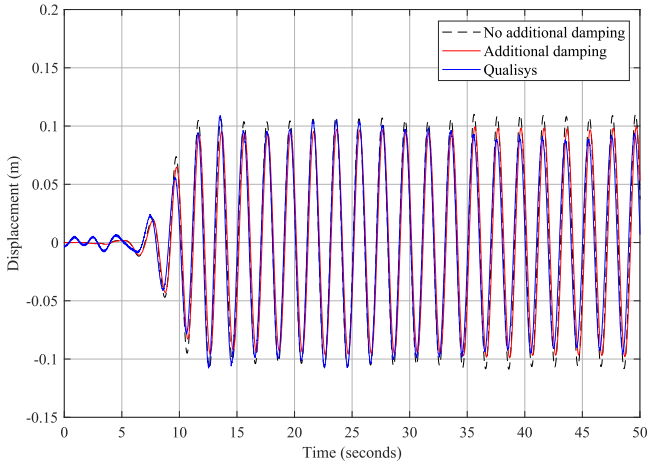

Fig. 8. Regular wave validation of the linear hydrodynamic model, showing the effects of the additional damping term introduced in (38).

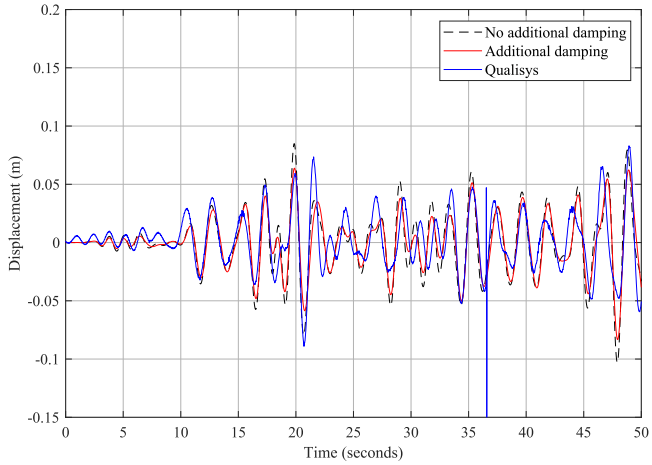

Fig. 9. Irregular wave validation of the linear hydrodynamic model, showing the effects of the additional damping term introduced in (38). Note the anomalous spike in magnitude at approximately 36 s, which is an indicator of a snatch load at this time step.

A. *Validation of Hydrodynamic Models*

Validation of hydrodynamic models is carried out by setting the wave probe measurements for free surface elevation as the input to the model and comparing the resultant model output with the Qualisys data for the heave displacement of the buoy. As the wave probe data were measured between the buoy and the wavemaker, cross correlation between the Qualisys heave data and the model output (which is also affected by the causalization delay) is used to align the two signals.

1) Sealed Moonpool: For the sealed moonpool case, the model output was found to be underdamped, when compared to the measured output. This could be due to a number of factors, as the linear model ignores the effects of air compressibility in the chamber, viscous drag force, and the dynamics of the mooring lines. To account for the underdamped response an additional damping term, b_{add}, is introduced to (21), giving the following:

$$A = \begin{bmatrix} A_e & 0 & 0 & 0 \\ 0 & A_{rc} & 0 & B_{rc} \\ 0 & 0 & 0 & 1 \\ \frac{C_e}{M^*_{33}} & \frac{C_{rc}}{M^*_{33}} & -\frac{c_{hs}}{M^*_{33}} & -\frac{b_{add}}{M^*_{33}} \end{bmatrix}$$

$$B = \begin{bmatrix} B_e \\ 0 \\ 0 \\ 0 \end{bmatrix} \quad x = \begin{bmatrix} Y_e \\ Y_{rc} \\ z_3 \\ \dot{z}_3 \end{bmatrix} \quad u = \eta. \tag{38}$$

This additional damping term is adjusted until the model output more closely matches the Qualisys measurements, as demonstrated in Fig. 8.

In irregular waves, the discrepancies between model output and the measured displacement are more noticeable. Although the additional damping term does show some improvement to the fit, there are still some discrepancies between the model output and the measured displacement, as shown in Fig. 9. One of the key drivers of such discrepancies is the existence of snatch loads from the moorings. In irregular wave tests, snatch loads, where the buoy reaches the end of its tether and is pulled back suddenly, were present in the measured heave data. These snatch loads present as large spikes in magnitude, and are an unfortunate artifact of wave tank testing in relatively shallow water with a short mooring line. This makes full validation of the model against irregular wave tests problematic, as the snatch loads have an impact on both the magnitude, and, more significantly, the phase of the device motion. Although snatch loads are also experienced by data buoys at sea, moorings are generally designed to minimise the incidence of snatch loads occurring, as they represent an extreme loading condition on the device. Potentially mooring dynamics could be included in the estimator model, and this could be a valuable area of future research. Furthermore, it was assumed that the waves measured by the waveprobes were identical to those experienced by the device. Unfortunately, in wave tank testing, small surface variations in the free surface do occur, and these are especially noticeable in irregular waves. Such variations are primarily driven by radiated waves from the device itself, and the reflections from wave tank walls. These effects from using real tank test data impose some limitations on verifying the effectiveness of the results obtained by the estimator, as discussed in Section IV-B1. For comparison, where ideal simulated irregular wave data was used in Section IV-B2, the estimator performed particularly strongly.

2) 25 mm Orifice Plate: With irregular test results unavailable for validating the nonlinear model representing the buoy with an orifice plate, the measured heave displacement in regular waves is compared to the model output, as shown in Fig. 10. It can be seen in Fig. 10 that a good match between the model output and the Qualisys data are achieved, without the introduction of any additional linear damping term. This suggests that the nonlinear model more fully captures the dynamics of the device, compared to the linear model. The effects of including air compressibility in the nonlinear model could also be compared at this stage, with air compressibility effects found to be negligible, as shown in Fig. 10.

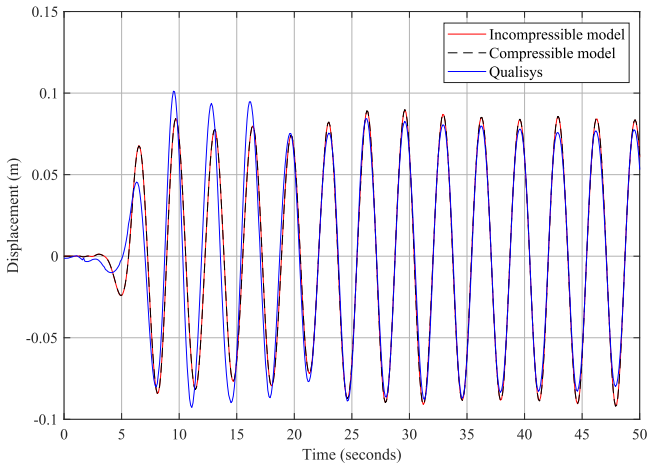

Fig. 10. Validation results comparing the heave displacement calculated by the 25-mm orifice plate model and the measured heave displacement from Qualisys. Note the imperceptible difference between the model accounting for air compressibility and the model assuming air incompressibility.

B. Estimation of Free Surface Elevation

To compare the estimated free surface elevation against the measured free surface, the causalization delay (2 s), along with any small delay introduced by the estimator structure itself (approximately 0.1 s), is removed from the estimated signal to properly align the two signals. With the estimated and measured signals aligned, the NRMSE is calculated as follows:

$$\text{NRMSE} = \sqrt{\frac{\sum_k |\eta_{\text{meas}}(k) - \tilde{\eta}^{\text{KFRW}}(k)|^2}{\sum_k |\eta_{\text{meas}}|^2}} \tag{39}$$

and used as a measure of GoF, given in percentage as $\%_{GoF}$

$$\%_{\text{GoF}} = 100(1 - \text{NRMSE}). \tag{40}$$

NRMSE is a highly sensitive measure of how two signals correlate, particularly with regards to phase. In irregular wave tests for the sealed buoy, a high incidence of snatch loads was observed, which interrupt the natural motion of the buoy, making an NRMSE comparison of the signals obtained difficult, due to a poor match in phase. To gauge whether the estimated values were close to the measured values on a more forgiving metric, the significant wave height and zero-crossing period of the estimated free surface were also compared. Calculating H_s from time series data is trivial, as it is simply the average of the highest 1/3 of the waves over the acquisition time. The zero-crossing period is found in the time domain by identifying the up zero-crossing indices of the time series and finding the average of the time between each up zero-crossing across the acquisition time.

As it is assumed the estimator will be used in seas where no prior information is known, all states within the estimator are initialized at 0.

1) Sealed Moonpool: The KFRW used with the sealed moonpool, being a fully linear model, was found to have a very fast execution time, even using MATLAB, which is known to be a slow interpreter, at approximately 0.020 s for a time series of 150 s, using time steps of 0.1 s (on a PC with Intel Core i7-1265 U and 32 GB RAM). This indicates the estimator ability to return estimates in real time, albeit, due to the causalization delay and the small inherent delay of the estimator itself, affected by a small delay.

Some tuning of the process noise covariance matrix, Q, is required for the estimator to work correctly. This matrix determines how much trust is put into each estimated state. In this case, more trust is put in the model states than in the state relating to the random walk, with the highest trust put in the state corresponding to the buoy displacement, as this is the state directly corresponding to the measured output. The measurement noise from the Qualisys data was found to be relatively small, with a corresponding measurement noise covariance value of $1e^{-6}$ used in the R matrix. In real applications, measurements of buoy motion would come from an onboard IMU, with R adjusted appropriately based on the sensor noise level of the IMU.

To analyze the estimator performance, an acquisition window of 20 s is used, across which values for T_z and H_s are obtained for both the measured and estimated free surface elevation. The GoF between the estimated signal and the measured signal is also calculated. Because all states are initialized at 0, the estimated free surface elevation undergoes a transient period before a steady state is reached. Therefore the acquisition window for any comparisons was set to be after any transients have settled, better representing the real sea application where the estimator would be expected to be free running for a long time. In irregular waves, any snatch loads were avoided when selecting the acquisition window.

A single acquisition window was used for the tests in regular waves, since once a steady state is reached there is little change in the motion of the device. The irregular wave tests were run for 1200 s, with a number of acquisition windows chosen to test the estimator against variations in free surface elevation over the test period.

Comparing free surface elevation results obtained by the linear estimator on a fully sealed buoy, against using the displacement of the buoy directly, shows that the behavior of the sealed buoy is close to that of a wave follower, particularly in regular waves, as demonstrated in Fig. 11.

In irregular waves, the presence of snatch loads reduces the accuracy of the obtained free surface wave elevation, particularly as it changes the relationship between the phase of the buoy and the waves. This means the GoF values for irregular waves were particularly poor, as NRMSE is highly affected by differences in phase. A comparison of the estimated and measured free surface elevation in irregular waves is shown in Fig. 12, again shown alongside the displacement of the buoy directly.

For regular waves, a GoF between 72% –82% is achieved, when comparing the estimated and the measured free surface elevation. In regular waves, the buoy heave motion was found to follow the free surface almost identically, as shown in the example in Fig. 11, with the difference slightly more noticeable in irregular waves, as shown in Fig. 12. To demonstrate the ability of the estimator to operate effectively, even after a significant number of waves have passed, Fig. 13 shows that the accuracy

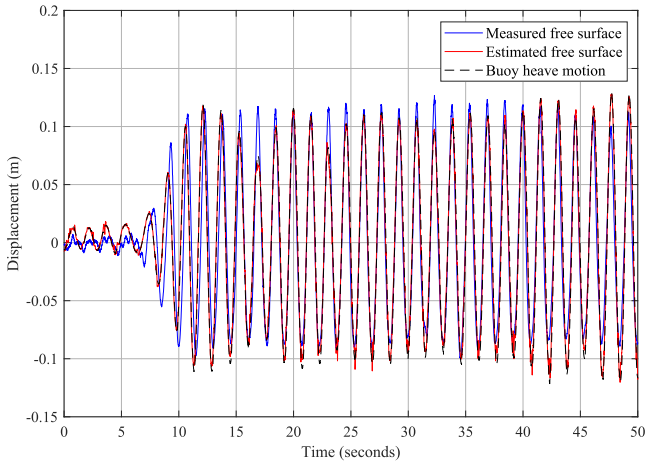

Fig. 11. Estimated free surface elevation in regular waves, for the buoy with a sealed moonpool, compared against the measured free surface, and the heave displacement of the buoy itself.

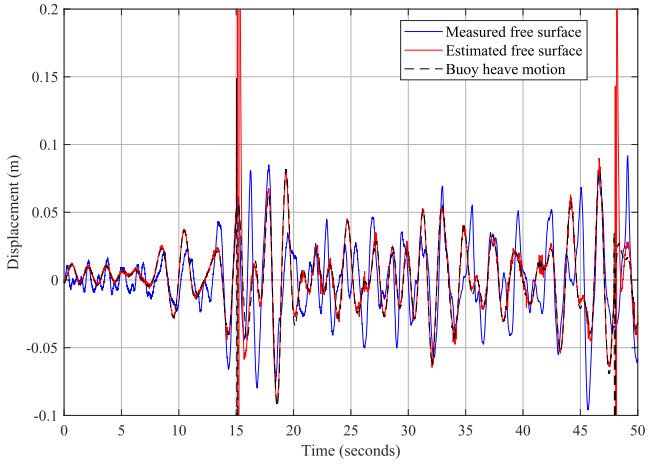

Fig. 12. Estimated free surface elevation in irregular waves, for the buoy with a sealed moonpool, compared against the measured free surface, and the heave displacement of the buoy itself. Again, note the presence of snatch loads at 15 and 48 s.

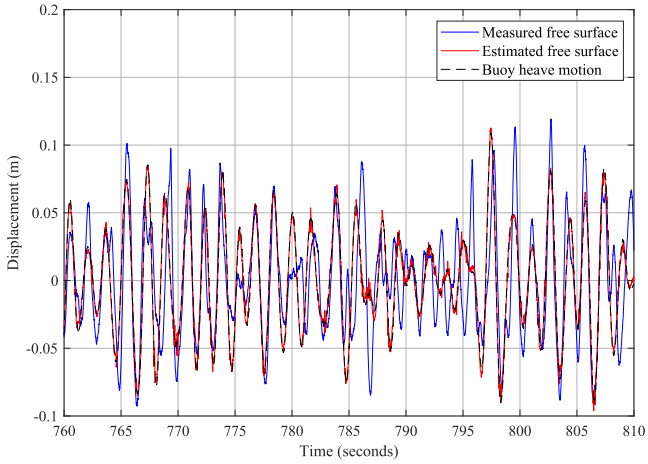

Fig. 13. Estimated free surface elevation in irregular waves, for the buoy with a sealed moonpool, as in Fig. 12; here showing performance after running for more than 12 min in irregular waves.

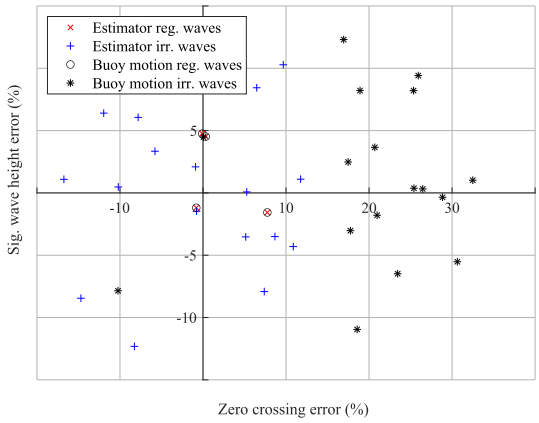

Fig. 14. Scatter plot showing the errors in obtaining T_z and H_s, for the buoy with a sealed moonpool, with positive errors showing overestimation, and negative errors showing underestimation.

of the estimator does not deteriorate over time. It should also be noted that the results shown in Fig. 14 used acquisition windows selected across the full 1200-s test time, which again did not show any deterioration in estimator accuracy.

A comparison between using the estimator and the buoy displacement directly, summarized in Fig. 14, shows that for a buoy whose behavior is close to a wave follower, there is no advantage to using the estimator in obtaining values for H_s, with both methods obtaining results approximately within a 10% error band of the measured H_s. The biggest difference, in the linear case, can be observed when comparing the obtained values for T_z in irregular waves, with the estimator capable of returning results with only around a 10% error, whereas directly using the heave measurements generally overpredicts T_z, in some cases by more than 20% .

2) 25-mm Orifice Plate: The state space model used to represent the 25-mm orifice plate was significantly larger in dimension than that for the sealed chamber, and combined with the nonlinearities introduced, it is unsurprising that the execution time using a MATLAB interpreter for the estimator in the nonlinear case is considerably slower, at 40–50-s execution time for a simulation time series of 150 s, using time steps of 0.1 s (on a PC with Intel Core i7-1265 U and 32 GB RAM).

The fast execution time is only possible with appropriate tuning of the process noise covariance matrix, Q. If Q is poorly tuned, the discretisation time needs to be reduced, in particularly poor tuning by up to 100 times, significantly increasing execution times. Poor tuning of Q, can also result in the estimated states tending to positive or negative infinity, as the system can become unstable. To ensure an estimator that is robust against these issues, a relatively high amount of trust must be put into all of the states within the estimator, in this case 0.1 for all states, except the random walk which is set to 1, and the buoy displacement which is set to 0.01. This tuning of Q was found to work across all test cases considered.

The results for validating the nonlinear estimator against experimental data can be seen in Fig. 15, clearly showing that the behavior of the buoy, when fitted with an orifice plate, is far from

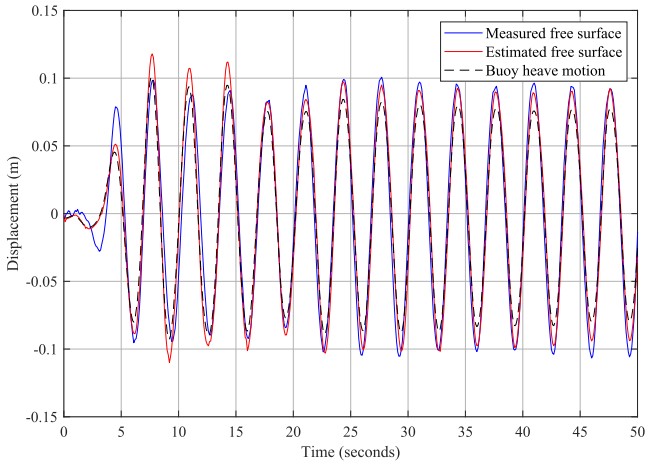

Fig. 15. Estimated free surface elevation in regular waves, for the buoy fitted with a 25-mm orifice plate, compared against the measured free surface, and the heave displacement of the buoy itself.

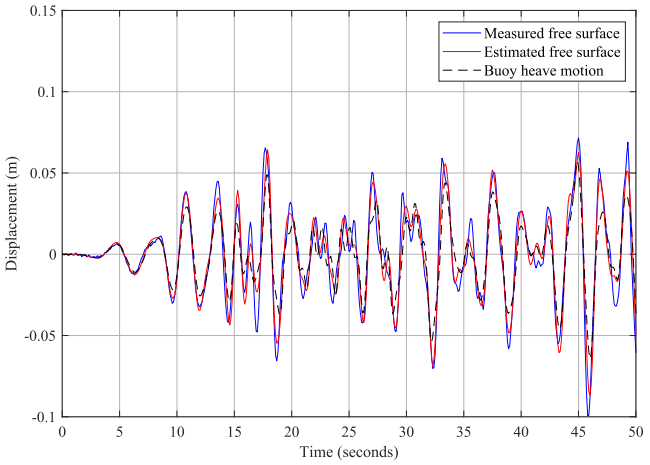

Fig. 17. Estimated free surface elevation in irregular waves, for the buoy fitted with a 25-mm orifice plate, compared against the measured free surface, and the heave displacement of the buoy itself.

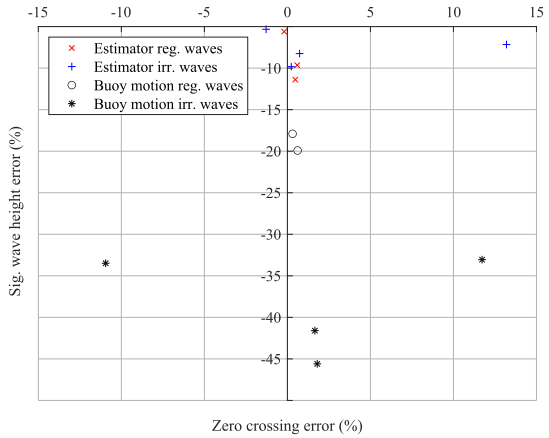

Fig. 16. Scatter plot showing the errors in obtaining T_z and H_s, for the buoy fitted with a 25-mm orifice plate, with positive errors showing overestimation, and negative errors showing underestimation.

that of a true wave follower. This makes the buoy fitted with an orifice plate fitted a significantly more compelling case for using a free surface estimator, and is more reflective of the dynamics of a wave powered data buoy. Fig. 15 clearly demonstrates the estimator ability to handle buoy dynamics, which are not representative of a true wave follower, able to return values for T_z and H_s within a 10% error band, as summarized in Fig. 16. The time series GoF obtained between the estimated and measured free surface elevation for the nonlinear estimator in regular waves is also high, at 60% –80%, depending on the particular test.

Unfortunately, no test data for the orifice plate are available in irregular waves. As discussed in Section IV-B1, the performance of the linear estimator in irregular waves is poorer than that in regular waves. Therefore, to gauge the nonlinear estimator performance in irregular waves, synthetic measurement data were produced, using experimental irregular wave measurements as the input to the hydrodynamic model fitted with an orifice plate, described in Section III-A2, and using the generated displacements as the measured output for the nonlinear estimator in irregular waves.

The resultant estimated free surface, for irregular waves, can be seen in Fig. 17. In the nonlinear case, a time series GoF of 73% –78% is achieved, with H_s and T_z estimates as accurate as those obtained in regular waves. This high accuracy is perhaps unsurprising, since Kalman filter-based estimators are highly model dependent, and with no discrepancies between the model used to generate the data and the model used in the estimator, and no unexpected changes in device motion due to snatch loads, it can be expected that the estimator will perform well. Nonetheless, the ability of the estimator to obtain accurate values for both time averaged parameters T_z and H_s, and time series free surface elevation, is demonstrated.

V. Conclusion

In this article, it is demonstrated that data buoys measuring wave parameters need not be constrained by the assumption that they must be true wave followers. This is most clearly demonstrated by the more realistic nonlinear case modeled, where an orifice plate emulates the effects of a turbine PTO, and the behavior of the buoy considered cannot be described as a wave follower. This study demonstrates that, through using a Kalman filter-based estimator, wave parameters T_z and H_s, alongside free surface elevation, can be successfully recovered from a data buoy, accounting for the dynamics of a simulated wave energy PTO.

Although the linear estimator, used in the fully sealed case with no PTO, was able to return accurate values for T_z, outperforming using the buoy displacement directly, there was no difference in accuracy between values obtained for H_s. As the fully sealed test case was found to be close to a wave follower, future work, using a controller with a PTO which can inject energy back into the system, such as a linear generator, could be used with the linear estimator to move the buoy further from being a wave follower, and demonstrate the estimator ability to handle the effects of energy maximizing control.

The addition of the orifice plate has a significant impact on the dynamics of the buoy, meaning measurements of the buoy motion directly are unable to return accurate values for either T_z or H_s. However, the estimator is generally able to recover these parameters to within a 10% error band of the measured values. This is similar to the current industry standard returned by wave followers of H_{mo}, showing it is entirely possible to use wave powered data buoys to measure wave parameters to the same accuracy as the wave followers currently in use. Furthermore, the ability of the nonlinear estimator to return accurate free surface elevation estimates, with a GoF between 70% –80% even in irregular waves, makes it suitable for measuring waves in applications where time series data are required.

Although this study does not use a data buoy directly powered by wave energy, the objective behind this study is to show that a Kalman filter-based soft sensor can be used to account for changes in dynamics that a wave energy PTO would introduce, in this case simulated via an orifice plate. The ability to handle changes to dynamics introduced by a simulated PTO, and still successfully return free surface elevation estimates, shows that wave energy could indeed be used to power data buoys. Furthermore, the ability of the estimator to return time domain free surface elevation data, at 0.1-s intervals, is a key strength of the Kalman filter-based estimator, with potential use in those applications where measuring only the statistical characteristic parameters of waves is not sufficient.

ACKNOWLEDGMENT

The authors would like to thank Yerai Peña-Sanchez, Marco Rosati, Pedro Fornaro, Facundo Mosquera, Ariádne Bertolin, and Hafiz Ahsan Said for the discussions with them.

REFERENCES

[1] M. D. Earle, "Nondirectional and directional wave data analysis procedures,," Nat. Data Buoy Centre (NDBC), United States of America Dept. Commerce, NDBC, Tech. Doc. 03-01, 2003, pp. 8–12.

[2] G. P. Nolan, J. V. Ringwood, and B. Holmes, "Short term wave energy variability off the west coast of Ireland," in *Proc. 7th Eur. Wave Tidal Energy Conf.*, Porto, Portugal, 2007, pp. 1–10.

[3] I. McLeod and J. V. Ringwood, "Powering data buoys using wave energy: A review of possibilities," *J. Ocean Eng. Mar. Energy*, vol. 8, pp. 417–432, 2022.

[4] J. V. Ringwood, G. Bacelli, and F. Fusco, "Energy-maximizing control of wave-energy converters: The development of control system technology to optimize their operation," *IEEE Control Syst. Mag.*, vol. 34, no. 5, pp. 30–55, Oct. 2014.

[5] C. Collins III, B. Lund, T. Waseda, and H. Graber, "On recording sea surface elevation with accelerometer buoys: Lessons from ITOP (2010)," *Ocean Dyn.*, vol. 64, pp. 895–904, 2014.

[6] S. Chakraborty, K. Ide, and B. Balachandran, "Missing values imputation in ocean buoy time series data," *Ocean Eng.*, vol. 318, 2025, Art. no. 120145.

[7] K. Budal et al., "The Norwegian wave-power buoy project," in *Proc. 2nd Int. Symp. Wave Energy Utilization*, Trondheim, Norway, 1982, pp. 323–344.

[8] A. Altunkaynak, "Adaptive estimation of wave parameters by Geno-Kalman filtering," *Ocean Eng.*, vol. 35, pp. 1245–1251, 2008.

[9] A. Altunkaynak and M. Özger, "Temporal significant wave height estimation from wind speed by perceptron Kalman filtering," *Ocean Eng.*, vol. 31, pp. 1245–1255, 2004.

[10] S. Küchler, J. Eberharter, K. Langer, K. Schneider, and O. Sawodny, "Heave motion estimation of a vessel using acceleration measurements," in *Proc. 18th IFAC World Congr.*, Milan, Italy, 2011, pp. 14742–14747.

[11] Ø. F. Auestad, J. T. Gravdahl, and T. I. Fossen, "Heave motion estimation on a craft using a strapdown inertial measurement unit," in *Proc. 9th IFAC Conf. Control Appl. Mar. Syst.*, Osaka, Japan, 2013, pp. 298–303.

[12] H. Øveraas, T. H. Bryne, and T. A. Johansen, "A linear time-invariant Kalman filter for estimating height in the presence of ocean waves," *Ocean Eng.*, vol. 320, 2025, Art. no. 120214.

[13] R. Pascoal and C. Guedes Soares, "Kalman filtering of vessel motions for ocean wave directional spectrum estimation," *Ocean Eng.*, vol. 36, pp. 477–488, 2009.

[14] R. Pascoal, L. Perera, and C. Guedes Soares, "Estimation of directional sea spectra from ship motions in sea trials," *Ocean Eng.*, vol. 132, pp. 126–137, 2017.

[15] H. Kim, H. Kang, and M.-H. Kim, "Real-time inverse estimation of ocean wave spectra from vessel-motion sensors using adaptive Kalman filter," *Appl. Sci.*, vol. 9, 2019, Art. no. 2729.

[16] H. Kim, J. Park, C. Jin, M. Kim, and D. Lee, "Real-time inverse estimation of multi-directional random waves from vessel-motion sensors using Kalman filter," *Ocean Eng.*, vol. 280, 2023, Art. no. 114501.

[17] JFC Marine, "Aids to navigation: Gannet buoys," Accessed, Sep. 21, 2024. [Online]. Available: https://jfcmarine.com/product/o1200-gannet-navigation-buoy/

[18] M. Boland, T. Kelly, R. Carolan, B. Walsh, and T. Dooley, "Scale model testing of the WASP - A novel wave measuring buoy," in *Proc. 13th Eur. Wave Tidal Energy Conf.*, Napoli, Italy, 2019, pp. 1531-1–1531-9.

[19] R. Carolan, B. Walsh, M. Boland, T. Dooley, and T. Kelly, "The design and construction of a prototype WASP - a novel wave measuring buoy," in *Proc. 13th Eur. Wave Tidal Energy Conf.*, Naples, Italy, 2019, Art. no. 1594.

[20] B. Walsh, R. Carolan, M. Boland, T. Dooley, and T. Kelly, "The use of air pressure measurements within a sealed moonpool for sea-state estimation," *J. Mar. Sci. Eng.*, vol. 12, 2024, Art. no. 2306.

[21] Y. Peña-Sanchez, C. Windt, J. Davidson, and J. V. Ringwood, "A critical comparison of excitation force estimators for wave-energy devices," *IEEE Trans. Control Syst. Technol.*, vol. 28, no. 6, pp. 2263–2275, Nov. 2020.

[22] T. Kelly, "Experimental and numerical modelling of a multiple oscillating water column structure," Ph.D. dissertation, Faculty of Sci. Eng., National Univ. Ireland Maynooth, Maynooth, Kildare, Ireland, 2018.

[23] D. V. Evans, "The oscillating water column wave-energy device," *IMA J. Appl. Math.*, vol. 22, pp. 423–433, Dec. 1978.

[24] T. Kelly, I. Zabala, Y. Peña-Sanchez, J. Ringwood, J. Henriques, and J. M. Blanco, "A post-processing technique for removing irregular frequencies and other issues in the results from BEM solvers," *Int. J. Mar. Energy*, vol. 5, pp. 123–131, 2022.

[25] R. G. Coe, G. Bacelli, and D. Forbush, "A practical approach to wave energy modeling and control," *Renewable Sustain. Energy Rev.*, vol. 142, 2021, Art. no. 110791.

[26] B. Guo, R. J. Patton, S. Jin, and J. Lan, "Numerical and experimental studies of excitation force approximation for wave energy conversion," *Renewable Energy*, vol. 125, pp. 877–889, 2018.

[27] Y. Peña-Sanchez et al., "Finite-order hydrodynamic approximation by moment-matching (FOAMM) toolbox for wave energy applications," in *Proc. 13th Eur. Wave Tidal Energy Conf.*, Naples, Italy, 2019, pp. 1448-1–1448-9.

[28] H. B. Bingham et al., "Ocean energy systems wave energy modeling task 10.4: Numerical modeling of a fixed oscillating water column," *Energies*, vol. 14, 2021, Art. no. 1718.

[29] S. Chen, "Orthogonal-least-squares forward selection for parsimonious modelling from data," *Engineering*, vol. 01, pp. 55–74, 2009.

[30] N. N. Narisetty, "Bayesian model selection for high-dimensional data," in *Principles and Methods for Data Science, Ser. Handbook of Statistics*, A. S. Srinivasa Rao and C. Rao, Eds., vol. 43. Amsterdam, The Netherlands: Elsevier, 2020, ch. 4, pp. 207–248.

[31] W. Sheng, R. Alcorn, and A. Lewis, "On thermodynamics in the primary power conversion of oscillating water column wave energy converters," *J. Renewable Sustain. Energy*, vol. 5, 2013, Art. no. 023105.

[32] J. V. Ringwood, S. Zhan, and N. Faedo, "Empowering wave energy with control technology: Possibilities and pitfalls," *Annu. Rev. Control*, vol. 55, pp. 18–44, 2023.

[33] D. García-Violini, N. Faedo, Y. Peña-Sanchez, V. Nava, and J. V. Ringwood, "Revisiting excitation force estimation in WECs: On the (MIS) use of structure-based estimation approaches," *Ocean Eng.*, vol. 311, 2024, Art. no. 118864.

Iain McLeod received the master's degree in electrical and mechanical engineering with international study from Strathclyde University, Glasgow, U.K., in 2018. He is currently working toward the Ph.D. degree in electronic engineering with the Centre for Ocean Energy Research, Maynooth University, Maynooth, Ireland, which he commenced in 2021.

His year of international study was spent with the University of Toronto, Toronto, Canada. After graduating, he worked on Rolls-Royce Civil Aerospace projects through Belcan, where he was employed as a Graduate Stress Engineer. His research focuses on using wave energy to power small-scale data buoys.

Mr. McLeod was the recipient of the BP Prize for best M.Eng. group project, for the group's replica of a mechanical television.

Brendan Walsh received the B.A. degree in mathematics, the B.A.I. degree in civil, structural and environmental engineering, the post graduate diploma in environmental engineering, the master's degree in engineering from Trinity College, Dublin, Ireland, in 2005, 2005, 2009, and 2012, respectively, and a Level 9 in teaching and learning from the Dundalk Institute of Technology (DKIT), Dundalk, Ireland in 2013. He is currently working toward the Ph.D degree in renewable engineering.

He is currently a Lecturer with the Civil Engineering Department, DKIT. His research focuses on the use of pressure measurements in a volume of air contained in a chamber above an oscillating water column (which is in communication with the ocean) to estimate the sea state incident upon the water column.

Mr. Walsh was the recipient of the title of Chartered Engineer by Engineers Ireland having previously worked in industry both in construction and consultancy as a Project Engineer on a variety of large-scale infrastructural works.

Thomas Kelly received the bachelor's degree in mechanical engineering, and the master's degree in renewable energy systems from the Dundalk Institute of Technology, Dundalk, Ireland, in 1997 and 2008, respectively, and the Ph.D. degree in electronic engineering from Maynooth University, Maynooth, Ireland, in 2018.

He is currently a Lecturer in engineering with the Dundalk Institute of Technology. His research focuses on all areas of renewable energy, with a particular focus on marine renewables.

Dr. Kelly is a Member of the Centre for Renewable Energy, Dundalk Institute of Technology, as well as an Honorary Research Fellow with the Centre for Ocean Energy Research, Maynooth University. He was the recipient of the HETAC Student of the Year Award.

John V. Ringwood (Fellow, IEEE) received the diploma degree in electrical engineering from the Dublin Institute of Technology, Dublin, Ireland, in 1981, and the Ph.D. degree in control systems from the University of Strathclyde, Glasgow, U.K., in 1985.

He is currently a Professor of electronic engineering with Maynooth University, Maynooth, Ireland, and the Director of the Centre for Ocean Energy Research, Maynooth University, Maynooth, Ireland. He is also a Chartered Engineer and a Fellow of Engineers Ireland. His current research interests include time series modelling, wave energy, and biomedical engineering.

Dr. Ringwood is in the Editorial Boards of the *Journal of Ocean Engineering and Marine Energy*, IEEE TRANSACTIONS ON SUSTAINABLE ENERGY, and *IET Renewable Power Generation*.